ORIGINAL PAPER

Effect of interaction between fluid and fault zone on triggering earthquakes in the shallow crust

Lifen Zhang[1] · Wulin Liao[1] · Yunsheng Yao[1,2] · Jinggang Li[1]

Abstract

Reservoir induced seismicity provides a suitable method for studying the roles of fluid in inducing earthquakes. The fault structure plays a predominant role in the occurrences of earthquakes, and the influences of fluid also cannot be disregarded. In this study, we investigate the active Fairy Mount fault in the Three Gorges Reservoir. Since water impoundment in 2003, more than 4000 detectable earthquakes have occurred along the fault. The vast majority of these earthquakes are associated with the fault and water impoundment. To explore the effects of water-fault interactions on induced earthquakes, a permeability structure of the fault zone is established by a series of geological experiments. Fault rocks, including unconsolidated breccias and fault gouges, collected from a presentative outcrop are employed for detailed microstructural and mineralogical analyses. The results reveal a complex internal fault structure and widespread fluid-rock interactions. The hydrogeological property of the fault exhibits a typical conduit/barrier permeability structure. Highly permeable damage zones act as fluid conduits for the infiltration of reservoir water to the subsurface, while the low permeable fault core renders the fault core as a potential fluids storage area to weaken the fault in the shallow crust. In sum, both the pore pressure changes due to water infiltration and the long-term chemical effect of water on the fault plane promote instability of the fault and induce earthquakes.

Keywords Three gorges reservoir · Induced earthquake · Internal fault structure · Permeability structure

Introduction

Since the 1930s, more than 130 reservoir induced seismicity cases have been reported in more than 40 countries (Gupta and Rastogi 1976; Gupta 2002; Gahalaut and Hassoup 2012; Ellsworth 2013; Grigoli et al. 2017; Gillian et al. 2018). The occurrence of reservoir induced earthquakes affects the operation of water conservancy projects to some extent. Therefore, a reasonable interpretation of the mechanism becomes very important in earthquake mitigation. In general, it is thought that geological structures provide tectonic conditions for induced earthquakes, and water plays an important triggering/inducing role (Gough and Gough 1970; Talwani and Acree

1985; Chen and Talwani 1998; El Hariri et al. 2010; Grigoli et al. 2017; Gillian et al. 2018). Reservoir induced earthquakes can be categorized into the fault rupture type and the collapse type (Chen and Talwani 1998; Kundu et al. 2015). In the fault rupture type, a preexisting fault is the controlling factor (Lei et al. 2008, 2013). The stress state of faults, hydraulic properties of fault rocks and connectivity of fluid pathways have considerable influences on induced earthquakes (Roeloffs 1988; Lei et al. 2008). When the stress of a fault accumulates to the peak strength of a new rupture, a small stress disturbance can accelerate ruptures to trigger earthquakes (Alt and Zoback 2017). Lei et al. (2008) investigated the triggering effects of the Zipingpu reservoir on the Wenchuan M8.1 earthquake and concluded that both water loading and pore pressure diffusion produced significant stress changes in the underlying seismogenic faults (Lei et al. 2008, 2013). Liu et al. (2011) noted that fault structures directly affected the pore pressure diffusion, which changed the process of reservoir induced earthquakes. Some numerical simulations were performed to study the effects of water on the fault stability based on simplified homogeneous fault models (Nascimento et al. 2004; Lei et al. 2008; Tao et al. 2015). However, the physical

✉ Lifen Zhang
   zhanglf112@163.com

[1] Key Laboratory of Earthquake Geodesy, Institute of Seismology, China Earthquake Administration, Wuhan 430071, China

[2] Institute of Disaster Prevention, Sanhe 065201, China

properties of fault rocks vary significantly across fault zones. Zhou et al. (2010) established a detailed geological model of the Longmenshan fault and suggested that composite permeability structure provided fluid channels to promote the Wenchuan earthquake. To understand the mechanisms of faults that interact with water in induced earthquakes, retrieval information about material composition and the permeability differences within fault zones is necessary.

The Three Gorges Reservoir, which is located in Yichang city, central China, is the largest water conservancy project in the world. Long-term water loading and infiltration have caused constant and irreversible changes in gravity, seepage, deformation and tectonic stress fields in the reservoir area and a remarkable increase in seismicity in the reservoir area (Yao et al. 2017). The earthquakes after impoundment were primarily clustered at the junction of the Fairy Mount fault and the Nine Brook fault, near the Gaoqiao fault and the Xietan mining areas (Fig. 1, Zhang et al. 2018). A majority of the earthquakes at the northern end of the Fairy Mount fault were closely associated with the fault structures (Fig. 1). Most studies explored the roles of water for increased seismicity (Chen et al. 2004; Li et al. 2009; Jiang et al. 2012; Hua et al. 2013; Luo and Ma 2016); however, detailed studies of the interaction between faults and water are lacking.

In this paper, we choose the Fairy Mount fault in the reservoir as our target. A systematic and detailed mineralogical, chemical and microstructural analysis of the fault zone is performed. Microstructures of bulk rocks and clay minerals provided important information about the fault zone architectures and fluid flow. The permeability structure of the fault zone is established. Based on the results, we further discuss the influence of water-fault interactions on induced earthquakes.

Geological setting and typical outcrop

The Three Gorges reservoir is narrow and long as shown in Fig. 1. The reservoir extends approximately 580 km in an east-west direction. Figure 1 provides a close-up view of the head region and highlights the geological/ geographical features and the distribution of the earthquakes. The head region is geologically located at the conjunction of the Yangtze platform and Qinling fold belt. The Huangling anticline and Zigui basin are two important tectonic units in the area (Yi et al. 2012). The Huangling anticline, which is composed of granite, diorite and a thick metamorphic complex of the former Sinian system, is characterized by high velocity anomaly with P wave velocity of 6.1–6.5 km/s (Li et al. 2009). The Zigui basin is primarily composed of Jurassic sandstone and mudstone. A low velocity anomaly appears at the depths of 0~5 km within the basin, which reflects the distribution of sedimentary caprocks (Li et al. 2009).

Triassic-Sinian carbonate rocks are extensively distributed in the remaining areas (Li et al. 2009). As shown in Fig. 1, there are three major fault systems existing in the head region, in which the NNW and NE-NNE-striking faults are more active (Yi et al. 2012).

The NNW-striking Fairy Mount fault is a representative active reverse fault, along which more than four thousand earthquakes of $M < 4.0$ have occurred since water impoundment in 2003. The fault lies to the west of the Huangling anticline (Fig. 1) and is divided into three subfaults: Fairy Mount fault, Duzhenwan fault and Qiaogou fault. Among the three subfaults, the northern Fairy Mount fault shown in the blue rectangle of Fig.1 is the most active fault. The Fairy Mount fault is approximately 21 km long and constitutes the west boundary of the Cretaceous sedimentary basin. The Huangkou outcrop is a typical geological profile of the northern subfault (Figs. 1 and 2). The outcrop is well exposed and systematically investigated, with a foot wall within the lower Cretaceous stratum, and a hanging wall that cuts through the Permian stratum (Fig. 2a and b). The fault zone at the outcrop consists of different units (Fig. 2b). Across the fault profile from east to west, the units are described as follows: purplish-red sandstone in the Cretaceous stratum on the foot wall dips SW with a steep dip angle (230 °/60 °). Near the fault plane, the host rocks fractured to fault breccias. The main fault zone dips SW with a dip angle of 75 °. Fault rocks consist of purplish-red breccias and lenses, and the widest part is approximately 1 m (Fig. 2b and c). The 20-cm-wide Green-grayish fault gouge attached to the hanging wall (Fig. 2b and d). In the tectonite, a compressive schistosity zone can be observed (Fig. 2e). Permian black-greyish limestone, dips to NE with a dip angle of 30 ° (Fig. 2a and d).

Sampling and analytical methods

Sampling

To determine the mineral composition and internal structure of the fault zone, we sampled at the Huangkou outcrop. First, a roughly 20 cm thick saprolite layer that covers the surface was carefully removed using a gardening scoop, after which the actual samples were collected. To provide reliable data about the spatial variation of rock properties, both the fault gouge and host rocks were sampled to preserve the microstructure and warrant sample representativity.

Fault gouges were sampled by inserting stainless steel tubes with an inner diameter of Ø25mm at a 1.5 mm wall thickness into the fault zone for approximately 250 mm parallel to the fault plane, to extract the enclosed material. Samples from the surrounding host rocks were collected by hammering. A total of nine samples were collected (Fig. 2b). The samples were numbered in sequence from the host rocks
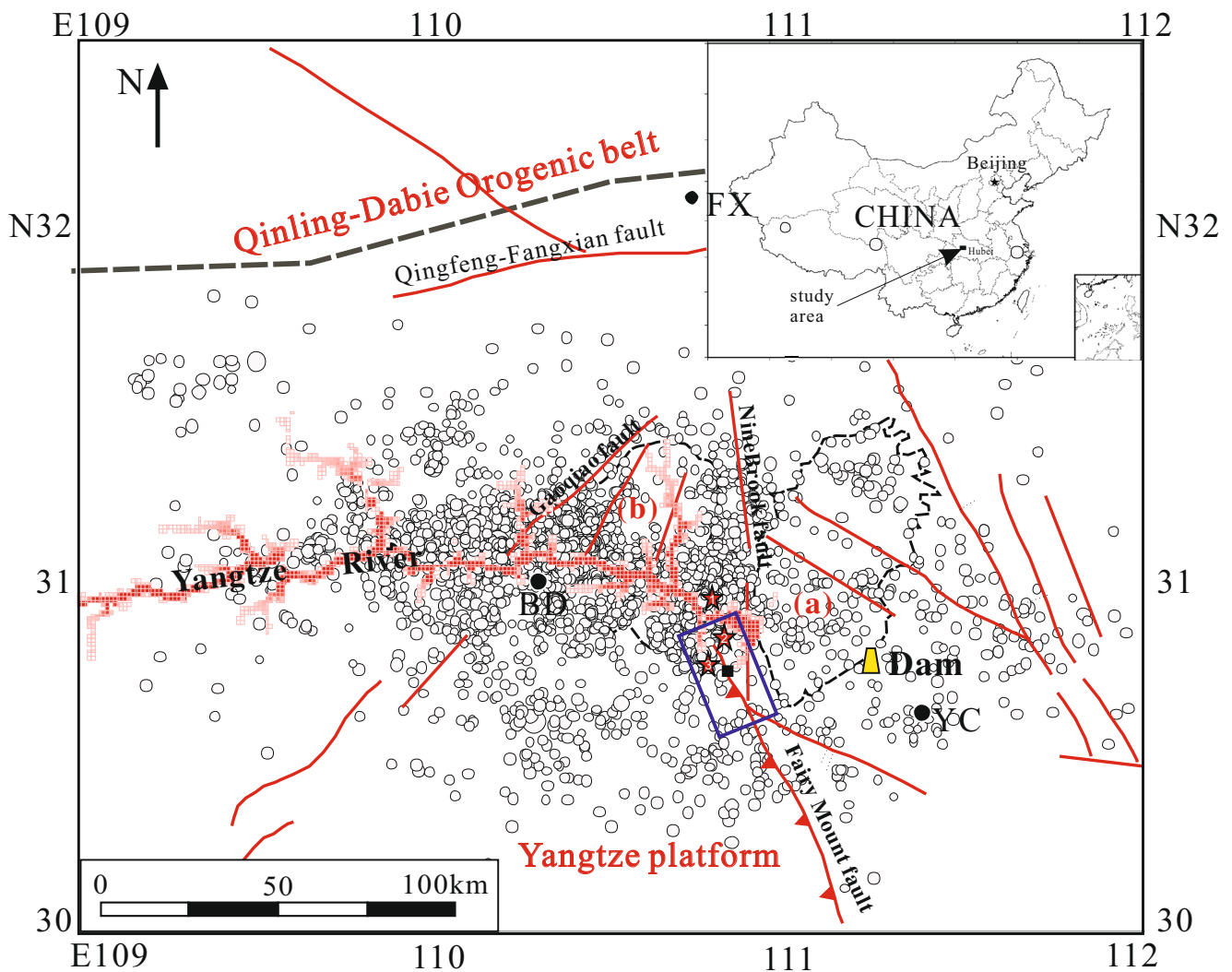
Fig. 1 Map view of location and geological and geographical features of the Three Gorges Reservoir and surrounding areas (modified after Zhang et al. 2019). Black dots denote major cities, red solid lines represent active faults, and black bold dashed lines show tectonic boundaries. (a) and (b) indicate the Huangling anticline and the Zigui syncline, respectively. The blue rectangle shows the target fault: Fairy Mount fault. White solid circles represent the earthquakes of M > 0.0 since water impoundment in 2003. Red stars show the locations of three earthquakes of M > 4.0

to the fault zone. In the outcrop, XHCR-1 and XHCR-2 were sampled from the host rocks, whereas the remaining samples were taken from the fault zone. Samples XH-2, XH-5 and XH-6 were collected from the purplish-red fault rocks, and samples XH-3, XH-4 and XH-7 were sampled from green-grayish fault rocks. Due to their very fine-grained nature, these samples are considered representative for the bulk whole-rock analysis.

Thin sectioning and optical petrography

All collected samples were carefully packaged and transported to the laboratory for sample processing and specimen preparation. Fault gouge samples were pushed out of the steel tubes in the laboratory using a stainless steel rod, and ~40 mm long contiguous portions suitable for thin sectioning were carefully

removed using a Stanley knife to protect the delicate microstructure. From the host rock samples, billets of 25 × 40 × 15 mm were cut using a water-cooled diamond blade. Gouge subcores and host rock billets were carefully dried at 35 °C before impregnation with epoxy (gouge only) and mounting on a standard petrographic carrier glass with dimensions of 27 × 47 mm. Mounted sample materials were lapped with even finer carborundum slurries to a final thickness of ~30 μm and finished with a standard 0.17 mm glass cover slip for optimal specimen preservation and viewing.

Thin sections were examined in a Zeiss AxioImager M2 m optical petrographic microscope in plane and cross polarized transmitted light. Micrographs were recorded with a Zeiss Axiocam 516 digital camera, and are presented in Figs. 3 and 6. Mineral modal contents of host rocks were determined by visual assessment cf. Folk (1951).
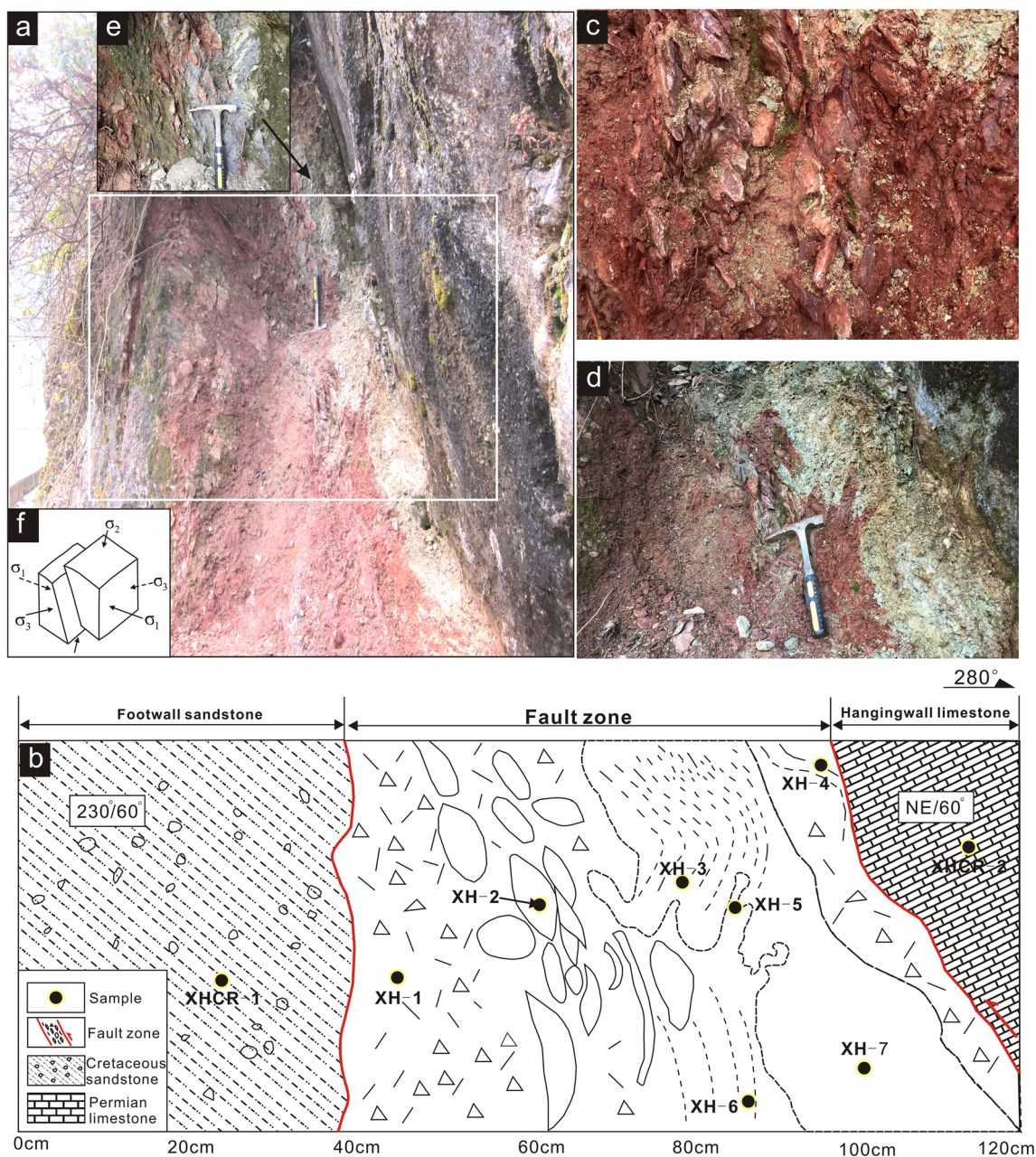
Fig. 2 **a** Photograph of the Huangkou outcrop. **b** The interpretive sketch of the fault zone traced from the white rectangle in (**a**). **c** is an enlarged the purplish-red fault lens. **d** shows an enlarged view of green-grayish fault gouge. **e** is a compressive schistosity zone. **f** shows the relationships between the fault and kinematics. σ_1, σ_2 and σ_3 represents the maximum, medium and minimum principal stress, respectively

In the figures and tables and their captions, mineral names are abbreviated according to the suggestions of Whitney and Evans (2010).

Bulk rock mineral modal content and identification of clay minerals

A mineral modal contents and semiquantitative analysis of clay minerals were performed by X-ray powder diffraction (XRPD).

The remaining materials after the thin sectioning of the gouge cores were first liberated by freeze-thaw cycling, then comminuted under acetone in an agate mortar and pestle. The bulk sample powder was mounted in a dimpled aluminum specimen holder and analyzed from 3 to 70 °2θ in 0.01 °2θ steps at 0.3 s counting time per step, with a total scan time of 33m30s. To determine the modal contents of minerals and the proportion of clay minerals present in vol%, diffractograms were indexed using proprietary Diffrac. Suite 4.0 software from Bruker AXS GmbH of Karlsruhe/DE.
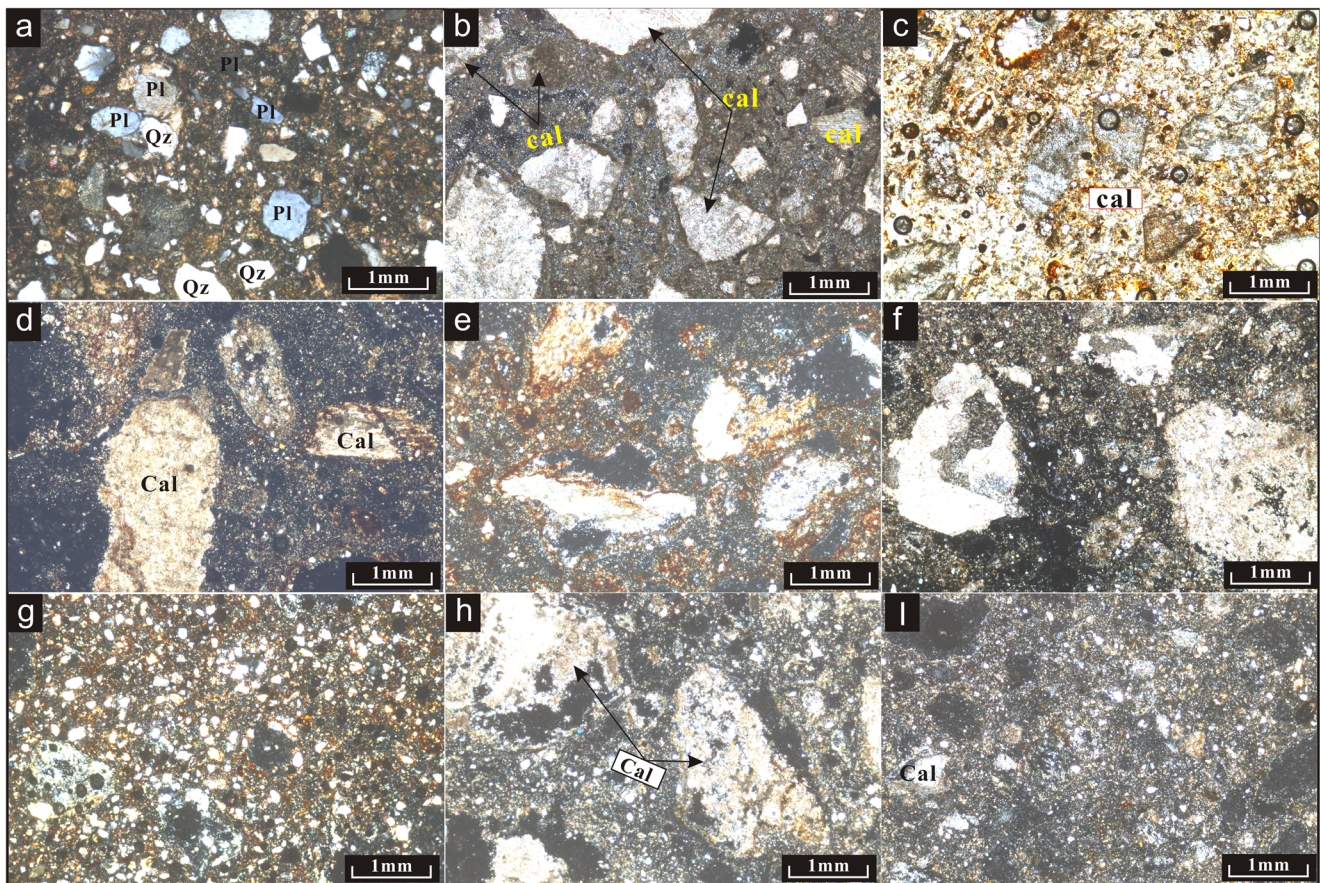
Fig. 3 Microstructures of different units of the Fairy Mount fault zone under an orthogonal microscope

For a detailed analysis, the clay fraction was prepared from gouge samples using Stokes segregation. After centrifuging in distilled water, suspensions with a particle size of <2 μm were deposited on glass slides. Thus, prepared oriented specimens were analyzed by XRPD from 3 to 35 °2θ in 0.01 °2θ steps at 2.0 s counting time per step, with a total scan time of 1h56m40s. Illite was distinguished from illite/smectite mixed layer after treatment with ethylene glycol. Kaolinite was distinguished from chlorite by heating at 550 °C.

All diffractograms were acquired on a Bruker D8 diffractometer operated at 40 kV and 40 mA, with a LynxEye digital detector using bulk CuKα radiation of λ = 1.54184 Å.

Bulk whole-rock geochemistry

A precisely weighed amount of 0.6 ± 0.0001 g of pulverized sample material below 75 μm (fault gouges and host rocks) was digested at ~1050 °C with 7× excess Li-metaborate in a Pt crucible. The glass bead was analyzed for main rock-forming elements in a Magix Pro 2440 X-ray fluorescence (XRF) instrument. Weight loss on ignition (LOI) was gravimetrically determined in a separate procedure. Main element contents are reported as oxides in wt%. The detection limits are stated per oxide in a separate column in the data tables.

Characteristics of the fault zone

Three units that consist of different rock types can be distinguished in the outcrop: contiguous host rock, fault breccia, and fault gouge at the center. Typical characteristics of these units are illustrated in Fig. 3.

Lithologies, mesostructure, microstructure

Host rock

The materials of the host rocks sampled from the hanging wall of the fault comprise purplish-red pebbly arkosic sandstone (Figs. 2and d, 3a). The sandstone conglomerates are typically clast-supported, coarse grained, with subrounded to subangular grain shapes and abundant pebble clasts (Fig. 2d). The pores only account for 2 wt%, which are predominated by intergranular pores and dissolution pores. The clastic debris account for 57%, and are composed of quartz, feldspar and rock debris. The remainings are filled with impurities composed of clay minerals and calcareous cements.

The host rocks of the foot wall comprise pure Permian limestone with high calcite content and small amounts of accessory minerals. Marl fragments with granular crystalline
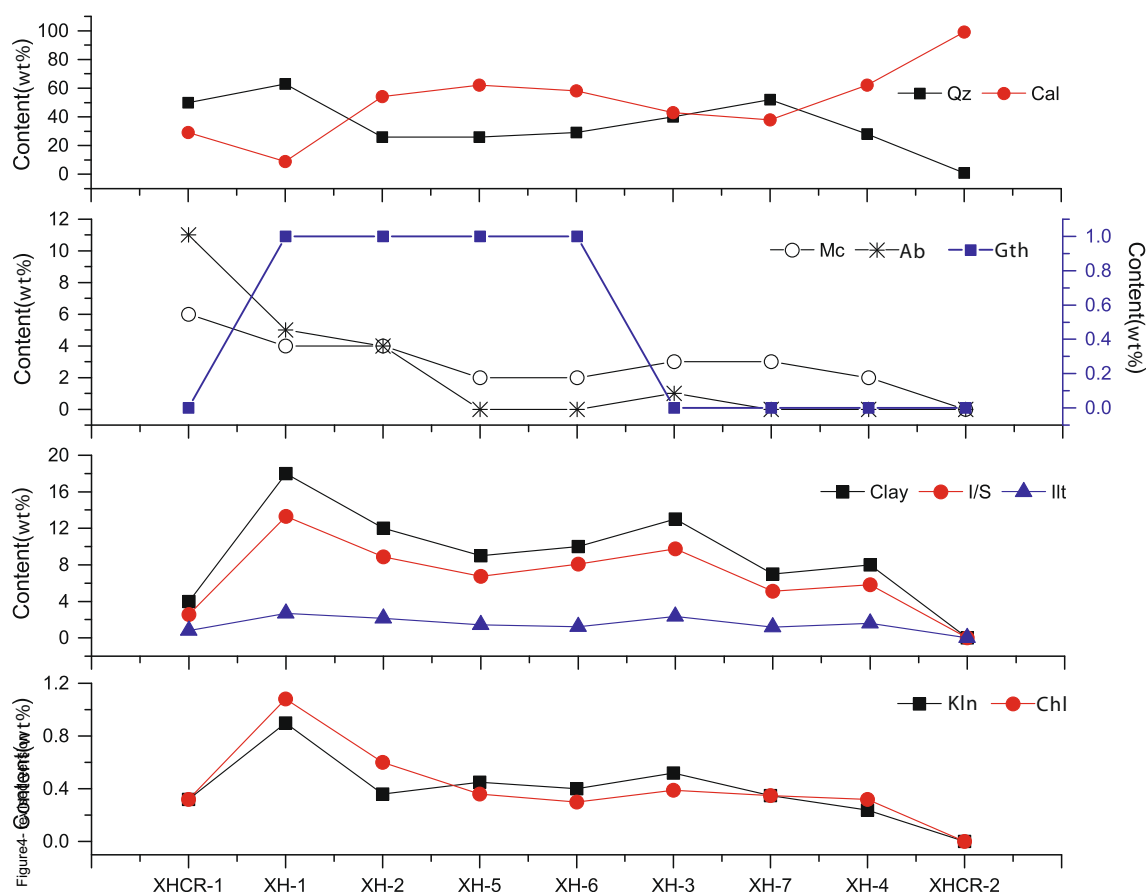
Fig. 4 Profiles of the bulk and clay mineral compositions of the Fairy Mount fault zone. Qz-Quartz, Cal-Calcite, Mc-Mircrocline, Ab-albite, Gth-Goethite, Sme-Smectite, Kln-Kaolinite, Chl-Chlorite, I/S-interlayer of illite and smectite

structure are visible under a microscope. This kind of structure is caused by recrystallization in the process of metamorphism, is formed by metasomatism and recrystallization in the presence of fluids, and has a special metasomatism structure of intact crystals. Metasomatic calcite can be observed, and the uniform extinction azimuth is presented under the cross-polarization (Fig. 3i).

Fault breccias

In the fault zone, the fault rocks with abundant joints and fissures are cut into rhombic structural lenses and tectonic breccias of different sizes under tectonic stress. The purplish-red fault lenses are clast-supported and have a sharp angular and irregular shape. The long-axis of the fault lenses intersects with the fault plane with an acute angle, which suggested that the fault had experienced a certain counterclockwise rotation and sliding (Fig. 2). Under a microscope, clay minerals are filled with the debris and recrystallization of minerals can be observed (Fig. 3c, d and e).

Green-grayish fault breccias cling to the hanging wall and show a granular structure (Fig. 2d). Calcite is the main component, which accounts for 77 wt%. The remaining consists of clay

minerals. The microstructure shows that some new minerals, such as chlorite and kaolinite, etc. can be observed (Fig. 3f).

Gouges

Purplish-red fault gouge presents a muddy structure under the microscope. The content of mud materials exceeds 70 wt%, in which fine debris with a size smaller than 0.0156 mm and clay minerals are the major components. Calcite and a small number of siliceous rocks can be observed (Fig. 3g). Green-grayish fault gouge that clings to the hanging wall has a brittle fractured debris with a subangular and subrounded structure, which is rich in calcite. The debris are composed of marl grains, few fine marl grains and siliceous rocks. The fine-grained material between the debris are composed of clay minerals, in which recrystallization of clay minerals is observed. Abundant solution pores are formed by the dissolutions of feldspar minerals (Figs. 3h and i).

Mineral assemblages of the fault zone

The X-ray diffraction measurement results show that the mineral compositions of the host rocks and fault rocks are different. In the footwall sandstone, quartz,
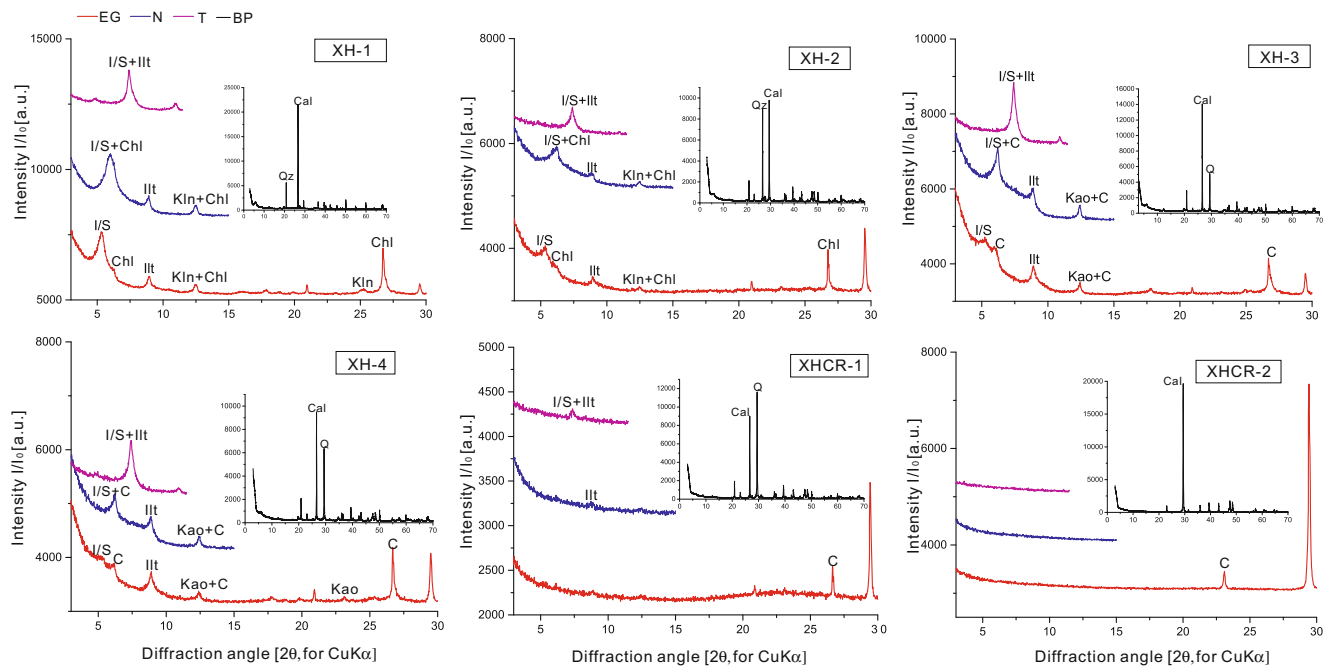
Fig. 5 X-ray diffraction patterns of the fault rocks. Black lines are the results from the bulk powder samples; and blue, red and pink lines are the results from air-dried, glycolated and heated clay samples (<2um) respectively. Qz-quartz, Pl-plagioclase, Ab-albite, Dol-dolomite, Cal-calcite, Sme-smectite, Chl-chlorite, Ilt-illite, Kln-kaolinite

calcite and feldspar are major minerals, which account for 50 wt%, 29 wt% and 17 wt%, respectively. The limestone sampled from the hanging wall is primarily composed of calcite, which represents a typical carbonate mineral assemblage. In the host rocks, clay minerals are present only in trace amounts..

Within the fault zone, the contents of clay minerals are distinctly higher than those in the host rocks. The clay minerals are composed of illite, kaolinite, chlorite and mixed-layer of illite/smectite. The concentration of the clay minerals across the fault profile exhibits an "M"-shape (Fig. 4). Purplish-red and green-grayish fault gouges are rich in clay minerals, such as samples XH-3, XH-5 and XH-7. Goethite is detected in the samples of XH-1, XH-2, XH-5 and XH-6, which explains the fault rocks that present a purplish-red color. The kaolinite and chlorite are primarily altered from the sandstone, which are abundant in samples XH-1 and XH-2. Across the profile, from the foot wall to the hanging wall, the calcite concentration increases. Conversely, the contents of quartz, microcline and albite show a decreasing trend (Fig. 4). The petrographic analyses clarify that the Fairy Mount fault zone is lithologically complex.

Discussion

Permeability architectures of the fault zone

The geological investigations show that the structure and composition of fault rocks across the fault zone vary considerably.

The footwall sandstone presents a grainy sandy structure, and the clasts are primarily composed of quartz, feldspar and calcite. They exhibit intermediate sorting, and have angular to sub-rounded morphology. The limestone on the hanging wall primarily comprises calcite, a small amount of quartz, feldspar and clay minerals. Within the fault zone, the samples have microfissures and the contents of clay minerals are higher than the host rocks (Figs. 4 and 5). Based on the differences in structures and material composition, the fault zone can be divided into fracture zone and fault core. The fracture zone refers to the subordinate structures of the rupture lens, breccias, fissures and secondary ruptures of the lateral fault of the fault nucleus. The fault core includes the fault-slip surface, purplish-red and green-grayish fault gouges.

The presented results show that the fracture zone is rich in quartz and feldspar, which has a good conductivity and is favorable for fluid infiltration. The fault core is mainly composed of clay minerals and unfavorable to water penetration (Duan et al. 2017). According to the scheme of the fault permeability structure in the low porosity brittle rock mass by Caine et al. (1996), the relative width of fault damage zone and fault core in the Fairy mount fault zone is approximately 0.5. The value suggests a combined conduit-barrier permeability structure (Caine et al. 1996). The permeability of the fault core is dominated by the grain-scale permeability of the fault rocks, whereas the permeability of the fracture zone is controlled by the hydraulic properties of the fracture network (Caine et al. 1996; Billi et al. 2003; Bense et al. 2013). Permeability data for natural fault gouges from the San
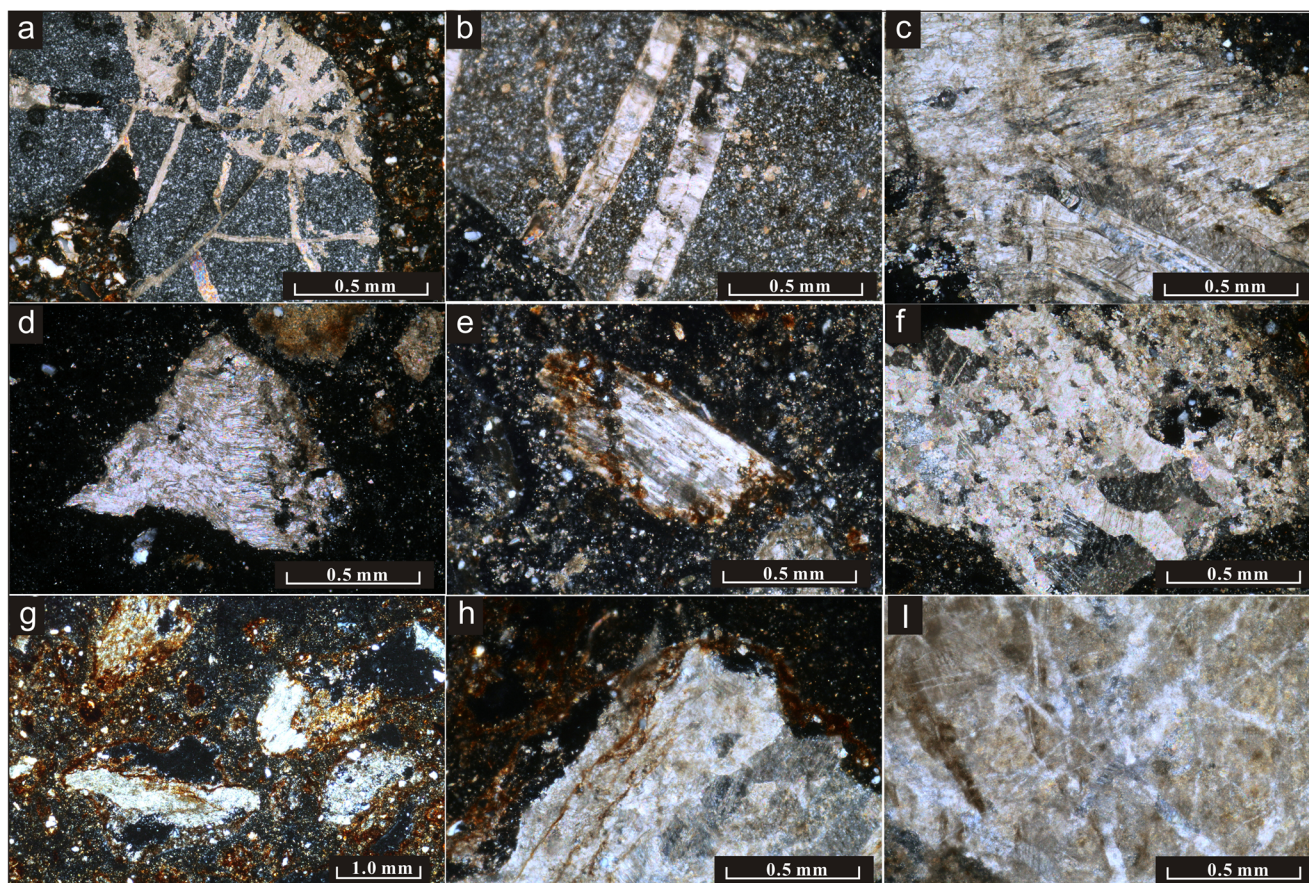
Fig. 6 Microstructures of the fault rocks in the Fairy Mount fault which indicats fluid activities. **a** Calcite veins in the siliceous rocks. **b** Calcite veins in siliceous rocks and dissolution pores in sample XH-3. **c** Twins bending and dissolution pores in sample XH-3. **d** Calcite bending twins in sample XH-2. **e** Iron dissemination and dissolution fissures in sample XH-5. **f** Fractured marble and alteration in sample XH-5. **g** Iron dissemination and dissolution pores in sample XH-6. **h** Fluid leaching and alteration, and iron dissemination in sample XH-7. **i** Calcite veins in sample XH-6

Andreas, Carboneras and Nojima Faults show values of 10^{-18} to 10^{-22} m^2, and the minimum is one order less than the experimental results achieved in the carbonate gouges (Wibberley and Shimamoto 2002). Morrow et al. (1981) revealed that the fault gouge has lower permeability than the fracture zone by measuring the permeability of fault rocks from the San Andreas fault. Evans et al. (1997) concluded that there was a permeability contrast between the fault core and the damage zone on the order of magnitude of 10~10^4, with a maximum contrast of 10^6 (Ganerod et al. 2008; Chen et al. 2013). The fault gouge may hinder fluid flow across the fault while the damaged zone may enhance flow parallel to the fault plane.

Fluid activity within the fault zone

Microstructural analyses of the fault rocks show that the calcite veins, fluid leaching and rock alteration characteristics are developed (Fig. 6). They provide extensive fluid migration pathways in the Fairy mount fault zone. Multiple calcite veins are presented in the siliceous rocks (Fig. 6a, b and i). In the early

stage of the fracture, micro-fissures formed; then gradually expanded together, and eventually macroscopic ruptures were formed. The fractures and fissures provided conduits for the fluid migration. The crystallization of the carbonate minerals formed the calcite veins (Fig. 6a, b and i), which are the products of the fluid activity (Ming et al. 2016). The fine-grained material mixed with debris are mainly composed of clay minerals, in which recrystallization of minerals is detected. The feldspar altered into the clay minerals; the dissolutions of the feldspar minerals produced dissolution pores (Figs. 6a, b and c). The recrystallization and dissolution pores all need the participation of fluid. In addition, the fluid that reacts with fault rocks caused the weathering and leaching effect (Lawther et al. 2016), which caused iron leaching (Fig. 6e, g and h). Our results suggested that a higher degree of fluid-rock interaction occurred in the fracture zone than that of the fault core.

The analysis of mineral composition shows that some hydrothermal minerals, such as goethite, exist in the shallow rupture zones (Fig. 4). This is a clear evidence of fluid activity in the fault zone. Across the fault profile, the feldspar content decreases. The decline in feldspar content in the green-grayish

Fig. 7 Distribution of springs and groundwater-observation wells along the Fairy Mount fault. Black solid rectangles labeled with w1, w2 and w3 represent the locations of the groundwater observation wells. Solid circles with tail show the location of the springs
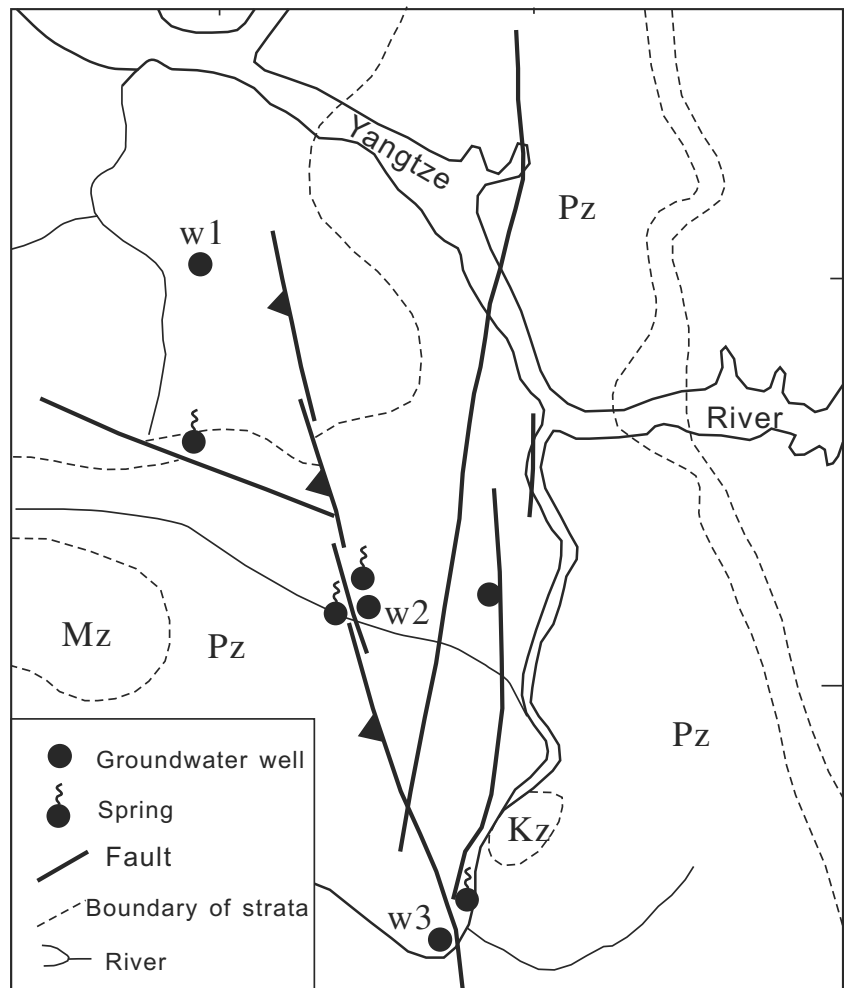
fault gouge suggested that the fault gouge underwent a water-rock reaction, in which the albite was broken down. The

outcrop basically reflects the characteristics of the shallow fault, and the fluid is extensively spread in the fault (Fig. 6).
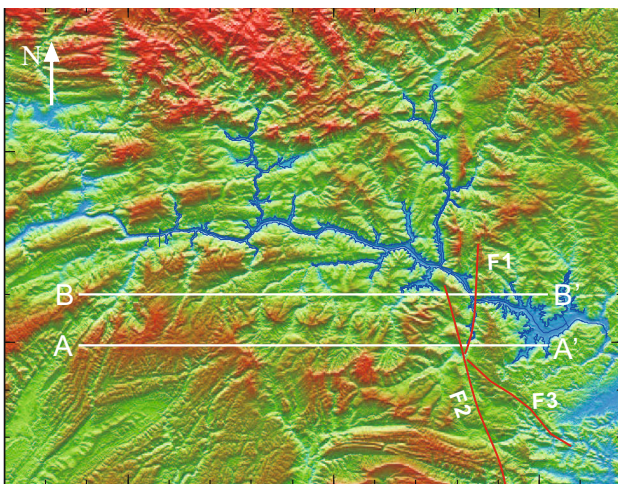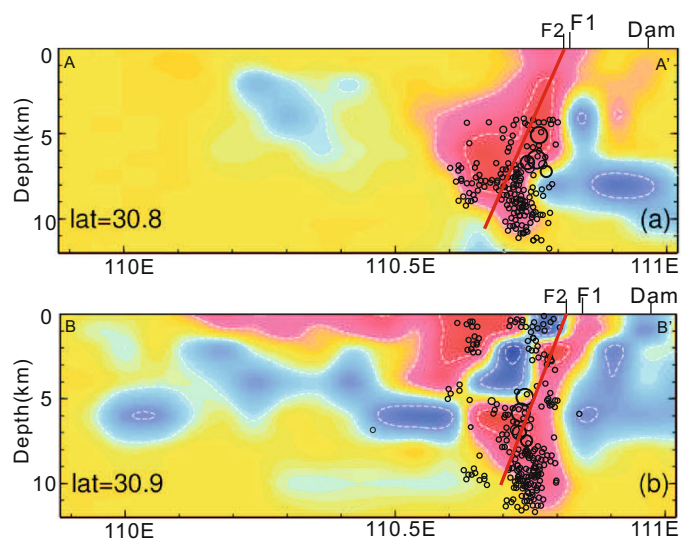

Fig. 8 Qs Tomography along the AA' profile and BB' profile in the Three Gorges reservoir (modified after Zhou et al. 2018) and the earthquake distribution. The red line denotes the Fairy Mount Fault, and black blank circles represent the earthquakes. In the scale, the blue scale and red scale show the high and low Qs values, respectively. F1 and F2 represents Fairy Mount fault and Nine Brook fault, respectively
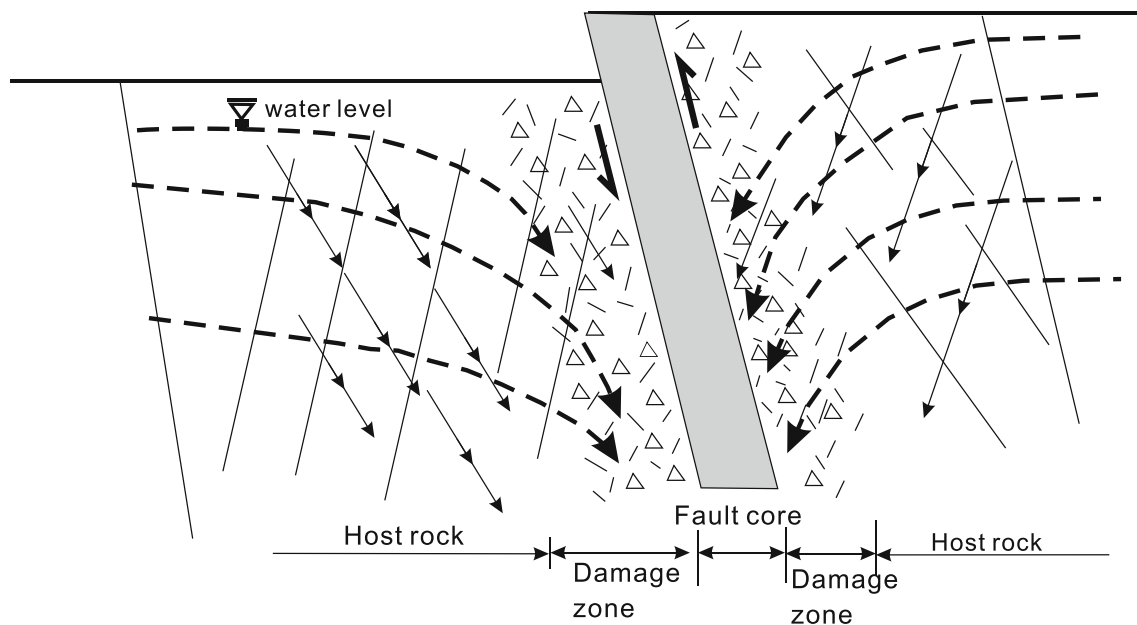
Fig. 9 Schematic of the permeability structure of the Fairy Mount fault and the earthquake mechanism induced by water-fault interaction

The fault has a direct hydraulic connection with the reservoir and is a conductive structure. The field investigation shows that there are some springs and ground-water observation wells along the fault (Fig. 7). The fluxes of wells W2 and W3 are 0.08 L/s and 6.3 L/s, respectively; near the wells, the fluxes of the ascending springs are 7.7 L/s and tens L/s, respectively. These springs and wells exhibit a rich flux and indicate significant ground water flow.

In addition to these geological evidences, seismic results obtained from other studies also proved the widespread fluid activity along the fault zone. Zhou et al. (2018) inferred a significant fluid infiltration at the intersection of the Fairy Mount fault and the Nine-brook fault from a very strong low Qs anomaly zone (Fig. 8). The anomaly zone dips to SW with a steep angle, which is in accordance with the characteristics of the Fairy mount fault (Fig. 8). Two seismic profiles showed that the earthquakes of $M > 2.0$ were primarily distributed along the low Qs anomaly zone from the shallow surface to a depth of 10 km (Fig. 8). The seismic activity also highlighted the water penetration along the fault.

A mechanism of fluid-induced earthquake

The reservoir is located on the foot wall of the fault. Theoretically, reservoir water loading will increase the normal stress and effective stress on the reverse fault, and make the fault more stable (Chen 2009). However, a large number of earthquakes occurred around the fault after water impoundment. How should we interpret the seismic activity? Previous studies indicated that an increase in pore pressure played an important role in triggering earthquakes (Talwani and Acree 1985; Gupta 2002). As shown in Fig. 9, the fault has a

composite conduit-barrier permeability structure and fluids extensively spread within the fault zone. Highly permeable damage zones act as fluid conduits for the infiltration of reservoir water to the subsurface. The fault core, which consists of fine-grained clay minerals, has a low permeability. The low permeability can restrain the fluid transport and render the fault core as a potential fluids storage area (Duan et al. 2017). During rapid seismic fault movement, the hydraulic property can prevent frictional heated fluids in the fault core from escaping and, consequently, increase the pore pressure to decrease the effective stress on the fault plane (Sibson 1977). It is a possible fault slip weakening mechanism in the shallow part (Duan et al. 2017). In addition, after the reservoir is impounded, pore pressure diffusion as a mechanism of stress transmission, increases pore pressure in the fractures as well (e.g. Nur and Booker 1972; Schloz et al. 1973, etc). There is a positive feedback between the pore pressure diffusion and rock failures (Masuda et al. 1990; Lei et al. 2011). The pore pressure diffusion may cause rock failures and the expansion of fractures, whereas the rock fractures can enhance the pore pressure diffusion. Frequent seismic activity as a result of the rock failures also substantially enhance the water infiltration within the fault fracture zone (Masuda et al. 1990; Lei et al. 2011).

The interaction between the fluid and the fault zone is very complex. With the exception that the physical mechanism is related with a decrease in the effective stress, the chemical effect is another important factor (Goddard and Evans 1995; Chen and Talwani 1998; Faulkner et al. 2010). The long-term chemical effects of fluid changed the material components of the fault zone, which caused the formation of the clay minerals and leaching and alteration of the materials in the fault zone.

Clay minerals, such as smectite, and illite/smectite layer, swell with water, and then soften and weaken the fault zone. That is, the chemical effect can decrease the friction strength of the fault and promote its instability.

The physical actions of fluid and the chemical effects caused failure and instability of the fault zone, which induced earthquakes. In addition, the occurrence of shallow microearthquakes caused the adjustment and concentration of stress at the tip of the fault. This led to fractures linkage, expansion of rupture volume, and accumulation of strain energy. In a certain geologic tectonic setting, this process may keep developing and induce large earthquakes. The migration mode and velocity of fluid in the fault zone are affected by the structure of the fault zone.

Conclusions

Since the water impoundment in 2003, more than four thousand detectable earthquakes have occurred along the Fairy Mount fault in the Three Gorges reservoir area. The geological investigations indicate that the fault has a composite conduit-barrier permeability structure, which is conducive for water infiltration. An abundance of calcite veins and iron leaching is evidence of widespread fluid activities in the fault zone. A low Q_s anomoly and the occurrences of a large number of earthquakes along the low anomaly zone also is strongly indicative of fluid ingress. The presented analyses suggested that interaction between fluid and the fault zone triggered the earthquakes. A decrease in the effective stress on the fault plane due to an increase in pore pressure is a predominant factor, and the chemical effects of water soften and weaken the fault by decreasing the friction strength.

A consensus on how fluids trigger earthquakes has not been reached. Although numerous methods explain the role of fluids, the long-term dynamic mechanism of fluid in stress transformation, fissure formation, fault slip, friction instability and strength changes of the fault zone remains ambiguous. In addition, the actual fault zone is very complex, and these mechanisms need to be tested and investigated for different fault zones.

References

Alt RC, Zoback MD (2017) In situ stress and active faulting in Oklahoma. Bull Seismol Soc Am 107(1):216–228

Bense VF, Gleeson T, Loveless SE, Bour O, Scibek J (2013) Fault zone hydrogeology. Earth-Sci Rev 127:171–192

Billi A, Salvini F, Storti F (2003) The damage zone-fault core transition in carbonate rocks: implications for fault growth, structure and permeability. J Struct Geol 25(11):1779–1794

Caine JS, Evans JP, Forster CB (1996) Fault zone architecture and permeability structure. Geology 24(11):1025–1028

Chen LY, Talwani P (1998) Reservoir-induced sesimicity in China. Pure Appl Geophys 153(1):133–149

Chen SJ, Su AJ, Luo DG (2004) Genesis and type of induced earthquake in Three Gorges reservoir. J Geod Geodyn 2:70–74

Chen R (2009) Did the reservoir impoundment trigger the Wenchuan earthquake? Sci China Ser D-Earth Sci 52:431–433

Chen JY, Yang XS, Ma SL, Spiers CJ (2013) Mass removal and clay mineral dehydration/rehydration in carbonate-rich surface outcrops of the 2008 Wenchuan Earthquake fault: geochemical evidence and implications for fault zone evolution and coseismic slip. J Geophys Res Solid Earth 118:474–496

Duan Q, Yang X, Chen J (2017) Hydraulic properties of a low permeable rupture zone on the Yingxiu-Beichuan Fault activated during the Wenchuan earthquake, China: Implications for fluid conduction, fault sealing, and dynamic weakening mechanisms. Tectonophysics 721:123–142

El Hariri M, Abercrombie RA, Rowe CA, do Nascimento AF (2010) The role of fluids in triggering earthquakes: observations from reservoir induced seismicity in Brazil. Geophys J Int 181(3):1566–1574

Ellsworth WE (2013) Injection-induced earthquakes. Science 341(6142): 1225942

Evans JP, Forster CB, Goddard JV (1997) Permeabilities of fault-related rocks and implications for fault-zone hydraulic structure. J Struct Geol 19(11):1393–1404

Faulkner D, Jackson C, Lunn R, Schlische R, Shipton Z, Wibberley C, Withjack M (2010) A review of recent developments concerning the structure, mechanics and fluid flow properties of fault zones. J Struct Geol 32:1557–1575

Folk RL (1951) A comparison chart for visual percentage estimation. J Sediment Petrol 21(1):32–33

Gahalaut K, Hassoup A (2012) Role of fluids in the earthquake occurrence around Aswan reservoir, Egypt. J Geophys Res 117:B02303

Ganerod GV, Braathen A, Willemoeswissing B (2008) Predictive permeability model of extensional faults in crystalline and metamorphic rocks; verification by pre-grouting in two sub-sea tunnels, Norway. J Struct Geol 30(8):993–1004

Gillian RF, Miles W, Gluyas J, Bruce RJ, Richard D (2018) Global review of human-induced earthquakes. Earth-Sci Rev 178:438–514

Goddard JV, Evans JP (1995) Chemical changes and fluid-rock interaction in faults of crystalline thrust sheets, northwestern Wyoming, USA. J Struct Geol 17:533–547

Gough DI, Gough WI (1970) Stress and deflection in the lithosphere near Lake Kariba. Geophys J Int 21:65–78

Grigoli F, Cesca S, Priolo E, Rinaldi AP, Clinton JF, Stabile TA, Dost B, Fernandez MG, Wiemer S, Dahm T (2017) Current challenges in monitoring, discrimination, and management of induced seismicity related to underground industrial activities: a European perspective. Rev Geophys 55(2):310–340

Gupta HK, Rastogi BK (1976) Dams and Earthquakes. Elsevier, Amsterdam, pp 1–229

Gupta HK (2002) A review of recent studies of triggered earthquakes by artificial water reservoirs with special emphasis on earthquakes in Koyna, India. Earth-Sci Rev 58(3/4):279–310

Hua W, Zheng SH, Yan CQ, Chen ZL (2013) Attenuation, site effects, and source parameters in the Three Gorges reservoir area, China. Bull Seismol Soc Am 103:371–382

Jiang HK, Song J, Wu Q (2012) Quantitative investigation of fluid triggering on seismicity in the Three Gorges reservoir area based on ETAS model. Chinese J Geophys 55(7):2341–2352 (in Chinese)

Kundu B, Vissa NK, Gahalaut VK (2015) Influence of anthropogenic groundwater unloading in Indo-Gangetic plains on the 25 April 2015 Mw 7.8 Gorkha, Nepal earthquake. Geophys Res Lett 42: 10607–10613

Lawther SE, Dempster TJ, Shipton ZK, Boyce AJ (2016) Effective crustal permeability controls fault evolution: an integrated structural, mineralogical and isotopic study in granitic gneiss, Monte Rosa, northern Italy. Tectonophysics 690:160–173

Lei XL, Yu G, Ma S, Wen X, Wang Q (2008) Earthquakes induced by water injection at ~3 km depth within the Rongchang gasfield, Chongqing, China. J Geophys Res 113:B10310

Lei X, Tamagawa T, Tezuka K, Takahashi M (2011) Role of drainage conditions in deformation and fracture of porous rocks under triaxial compression in the laboratory. Geophys Res Lett 38(24):L24310

Lei X, Ma S, Chen W, Pang C, Zeng J, Jiang B (2013) A detailed view of the injection-induced seismicity in a natural gas reservoir in Zigong, southwestern Sichuan Basin, China. J Geophys Res 118(8):4296–4311

Li Q, Zhao X, Cai JA, Liu RF, Long GH, AN YR (2009) P wave velocity structure of upper crust in Three Gorges Reservoir region of the Yangtze River. Sci China Ser D-Earth Sci 39(4):427–436

Liu YW, Xu LQ, Yang DX (2011) Pore pressure diffusion characteristics of Longtan reservoir-induced-earthquake. Chin J Geophys 54(4): 1028–1037 (in Chinese)

Luo JH, Ma HT (2016) A preliminary study on upper crustal velocity structure in the Three Gorges reservoir area. Seismology and Geology 38(2):329–334 (in Chinese)

Masuda K, Nishizawa O, Kusunose K, Satoh T, Takahashi M (1990) Positive feedback fracture process induced by nonuniform high-pressure water flow in dilatant granite. J Geophys Res 95(B13): 21583–21592

Ming X, Liu L, Yu M, Bai H, Yu L, Peng X, Yang T (2016) Bleached mudstone, iron concretions and calcite veins: A natural analogue for the effects of reducing CO_2-bearing fluids on iron migration and mineralization, sealing properties and composition of mudstone cap rocks. Geofluids 16(5):1017–1042

Morrow C, Shi LQ, Byerlee J (1981) Permeability and strength of San Andreas fault gouge under high pressure. Geophys Res Lett 8(4): 325–328

Nascimento AF, Lunn RJ, Cowie PA (2004) Numerical modelling of pore-pressure diffusion in a reservoir-induced seismicity site in northeast Brazil. Geophys J Int 160(1):249–262

Nur A, Booker JR (1972) Aftershocks caused by pore fluid flow? Science 175:885–887

Roeloffs E (1988) Fault stability changes induced beneath a reservoir with cyclic variations in water level. J Geophys Res 93:2107–2124

Schloz CH, Sykes LR, Aggarwl YP (1973) Earthquake prediction: A physical basis. Science 181:803–810

Sibson RH (1977) Fault rocks and fault mechanisms. J Geol Soc 133: 191–213

Talwani P, Acree S (1985) Pore Pressure Diffusion and the Mechanism of Reservoir-induced Seismicity. Pure Appl Geophys 122:947–965

Tao W, Masterlark T, Shen Z, Ronchin E (2015) Impoundment of the Zipingpu reservoir and triggering of the 2008 Mw 7.9 Wenchuan earthquake, China. J Geophys Res 120(10):7033–7047

Whitney DL, Evans BW (2010) Abbreviations for names of rock-forming minerals. Am Mineral 95:185–187

Wibberley CA, Shimamoto T (2002) Internal structure and permeability of major strike-slip fault zones: the Median Tectonic Line in Mie Prefecture, Southwest Japan. J Struct Geol 25:59–78

Yao YS, Wang QL, Liao WL, Zhang LF, Chen JH, Li JG, Yuan L, Zhao YN (2017) Influences of the Three Gorges project on seismic activities in the reservoir area. Sci Bull 62:1089–1098

Yi LX, D Z, CL L (2012) Preliminary study of reservoir-induced seismicity in the Three Gorges reservoir, China. Seismol Res Lett 83(5): 806–814

Zhang LF, Li JG, Sun XD, Liao WL, Zhao YN, Wei GC, He CF (2018) A possible mechanism of reservoir-induced earthquakes in the Three Gorges Reservoir, central China. Bull Seismol Soc Am 108(5B): 3016–3028

Zhang LF, Lei XL, Liao WL, Li JG, Yao YS (2019) Statistical parameters of seismicity induced by the impoundment of the Three Gorges Reservoir, Central China. Tectonophysics 751:13–22

Zhou B, Xue SF, Deng ZH, Sun F, Jiang HK (2010) Relationship between the evolution of reservoir-induced seismicity in space-time and the process of reservoir water body load-unloading and water infiltration—a case study of Zipingpu reservoir. Chin J Geophys 53(11):2651–2670

Zhou LQ, Zhao CP, Luo J, Chen ZL (2018) A detailed insight into fluid infiltration in the Three Gorges reservoir Area, China, from $3DV_P$, V_P/V_S, Q_P and Q_S Tomography. Bull Seismol Soc Am 108(5B): 3029–3045